CHAPTER 1

INTRODUCTION

1.1 Motivation

Over the past decades, the flow and heat transfer associated with a high speed jet impinging onto a heated flat plate have been the subject of many investigations because of its superior heat transfer capability. The advantage of the highly efficient jet impinging cooling has been applied to improve the drying of textiles and paper products, tempering of glasses and metals, cooling of gas turbine blades and microelectronic equipments, freezing of tissue in cryosurgery, etc.

However, for applications such as growth of semiconductor thin crystal films on heated silicon wafers through the chemical vapor deposition (CVD) processes and rapid thermal processing (RTP), low speed impinging jets are often employed. For a low speed jet the buoyancy generated by the heated wafer can be relatively high compared with the jet inertia and the buoyancy driven flow recirculation tends to appear. In order to obtain good deposition uniformity and high quality thin films, the flow in the CVD processing chamber needs to be stable and contains no vortices. Thus the understanding and analysis of the vortex flow characteristics in the low speed impinging jet flow need to be delineated.

It has been known that the vortex flow in the CVD processing chamber is manly affected by the jet inertia, the buoyancy force due to the heated wafer, and the geometry of the chamber. Besides, at increasing jet-disk separation distance, the buoyancy driven vortex flow becomes relatively strong since the Rayleigh number is proportional to H^3. In the mean time the inertia driven vortex flow is stronger and occupies a larger region for a larger H. Thus the interactions between the inertia and buoyancy driven vortex flows are expected to be more intense. Obviously, shortening

the jet-disk separation distance is beneficial in suppressing the flow recirculations. But a small jet-disk separation distance is more likely to cause unwanted vapor deposition on the jet nozzle and top wall of the processing chamber. In the present study, we intend to unveil the characteristics of the vortex flow in a low speed jet impinging onto a horizontal heated disk confined in a vertical cylindrical chamber with a larger jet-disk separation distance ($HD_j = 4 \sim 6$).

1.2 Literature Review

The flow in a jet impinging vertically onto a plate can be divided into three regions as illustrated in Fig. 1.1 [1] : (1) free jet region: near the nozzle the jet flow mainly moves in the axial direction and is not affected to a noticeable degree by the presence of the impingement surface, (2) stagnation region: near the geometric center of the target plate, the jet impinges the plate and then changes in the flow direction, (3) wall jet region: away from the stagnation region but near the target plate the transverse velocity rises rapidly to a maximum near the wall and then falls at greater distance from the wall. More complete information on various aspects of the flow and heat transfer associated with the impinging jets can be found from the critical reviews by Jambunathan et al [2], and Viskanta [3]. According to the turbulence intensity measurement at a nozzle exit, Lin et al. [4] suggested that the jet at a Reynolds number smaller than 1,226 may be regarded as in an 'initially' laminar flow regime. It also revealed that the intensity of turbulence increased continuously with the distance measured from the nozzle exit.

Considerable amount of work has been carried out in the past to investigate the fluid flow and heat transfer in the round or slot jet impinging onto a large horizontal plate. Most of the studies focus on quantifying the highly efficient heat transfer associated with the high speed impinging jets. Thus the flow driven by the jet inertia

is considerably stronger than the buoyancy driven flow due to the heated plate in the turbulent impinging jet. To explore the detailed vortex flow structure, Fitzgerald and Garimella [5] and Morris et al. [6 & 7] used numerical simulation and flow visualization to investigate the vortex flow characteristics for a liquid impinging jet, which were found to be influenced by the jet Reynolds number Re_j and jet-disk separation distance H . They pointed out that the center of the inertia driven vortex roll moved away from jet axis at increasing Re_j and H. Heat transfer in the turbulent impinging jet was numerically prdicted by Colucci and Viskanta [8], Gao and Ewing [9], and Narayanan et al. [10]. Colucci and Viskanta [8] reported the effects of a hyperbolic nozzle outlet on the local heat transfer. The numerical prediction from Gao and Ewing [9] revealed that the upper plate confinement did not exhibit noticeable effect on the heat transfer for the ratio of the jet-disk separation distance to the jet diameter greater than 1. Angioletti et al. [11] conducted an experiment to examine transitional impinging jets without confined plate for $1{,}000 < Re_j < 4{,}000$. Their results showed that the local heat transfer was strongly influenced by the impinging jet structures. Specifically, the maximum heat transfer coefficient offset was noted to result from the induced large-scale toroidal vortices near on the plate. Furthermore, heat transfer in a confined impinging slot jet covering the laminar and turbulent regimes was studied by Park et al. [12].

Recently, the vortex flow structures resulting from a low speed gas jet impinging onto a heated horizontal disk confined in a vertical cylindrical chamber at low Re_j were visualized by Hsieh et al. [13]. They showed that the gas flow recirculation was typically in the form of three circular vortex rolls including a primary vortex roll around the jet, a secondary vortex roll in the middle region and a buoyancy-induced vortex roll in the outer zone of the chamber. The inner and middle vortex rolls are driven by the viscous shear due to the nonuniform velocity distribution in the jet and

are stronger and bigger at a high Re_j. The secondary inertia-driven vortex roll only appears at certain high Re_j and is much smaller and weaker than the primary inertia-driven vortex roll. The buoyancy driven outer vortex roll results from the temperature difference between the heated disk and inlet gas and is important at high buoyancy-to-inertia ratio. In addition to the appearance of vortices, the effects of the jet Reynolds number and jet-disk separation distance on the locations of the centers of the primary and secondary vortex rolls were investigated by Law and Masliyah [14]. Details on the size and locations of the inertia driven primary and secondary vortex rolls affected by the jet Reynolds and Richardson numbers for a laminar confined slot-jet were examined by Sahoo and Sharif [15]. Moreover, the effects of the jet-disk separation distance on the vortex flow patterns were investigated by Hsieh and Lin [16] for $HD_j \leq 3$. They reported the size and onset of the inertia and buoyancy driven vortex rolls affected by HD_j. Moreover, the critical condition for the onset of the inertia driven time dependent flow for the unheated disk was also provided. For a confined laminar slot impinging jet the critical jet Reynolds number for the onset of unsteady flow was numerically shown to be between 585 and 610 by Chiriac and Ortega [17]. Santen et al. [18 & 19] indicated that the onset of thermal instability became earlier at increasing buoyancy-to-inertia ratio. Chung and Luo [20] suggested that unsteady heat transfer in a impinging jet was strongly dependent on the vortex dynamics. Moreover, a laminar impinging jet with small pulsation at the outlet of the jet was numerically simulated by Poh et al. [21]. They showed that in a periodic cycle the large vortice appearing in the minimum velocity state was broken into two smaller vortices when the flow was accelerated sinusodially to arrive at the maximum velocity state, after which the two vortices merged again when the flow was decelerated back to the minimum velocity state. Hsieh et al. [22] and Law and Masliyah [23] found that the impinging jet flow structure was significantly influenced by the chamber

geometry. Specifically, Hsieh et al.[22] revealed that inclining the chamber top could effectively suppress the buoyancy-induced vortex flow at low buoyancy-to-inertia ratios and the unsteady vortex flow oscillation could be completely stabilized even at high buoyancy-to-inertia ratios. Lin [24] provided the measured data for the heat transfer coefficient varied with the jet Reynolds number and the jet-disk separation distance in the laminar and transitional impinging jets. Chou and Hung [25] suggested that the parabolic velocity profile at the jet outlet had a maximum stagnation Nusselt number. In a recent flow visualization study for HD_j ranging from 1.0 to 3.0 and Re_j up to1,623, Hsieh et al. [26] reported that at sufficiently high Re_j the vortex flow became unstable due to the inertia-driven flow instability. Only for $HD_j = 2.0$ the flow is subjected to a simultaneous presence of the inertia and buoyancy driven instability. It is also noted that the critical Re_j for the onset of time dependent flow increases with ΔT for $HD_j = 1.0$ & 2.0 but for $HD_j = 3.0$ the opposite is true.

As mentioned above, in the impinging jet flow confined in a chamber encountered in the chemical vapor deposition (CVD), the gases impinging to the CVD chamber are at relatively low flow rates and the buoyancy in the flow is no longer small compared with the jet inertia with the Reynolds and Rayleigh numbers respectively ranging from 0.01 to 100.0 and from 10000 to 1000000. The importance of the buoyancy on the recirculating flow in a vertical CVD reactor was demonstrated by Wahl [27]. Similar investigations have been carried out for various types of the MOCVD reactor [28-30]. A numerical simulation from Van Santen et al. [31] showed that the symmetry breaking of the jet flow owing to the buoyancy effects may occur in an axi-symmetric CVD reactor with $HD_j \geq 1.0$. Recently, Vanka and his colleagues [32 & 33] conducted a series of computational studies to explore the effects of the flow rate, substrate rotation rate, and chamber geometry on the flow in impinging jet CVD reactor. In examining deposition of particles by a confined impinging jet at $Re_j =$

10,000 Burwash et al. [34] reported that increasing the ratio of the jet-disk separation distance to the jet diameter from 2.0 to 6.0 could result in higher deposition efficiency and deposition density around the stagnation point on a wafer. It also revealed that the deposition of the particles mainly resulted from turbulent dispersion for $HD_j = 2$ and the jet inertia driven particle impact on the wafer became more important for $HD_j = 4$ & 6.

1.3 Objective and Scope of Present Study

The above literature review clearly indicates that although considerable works have been carried out to study the flow and thermal characteristics in a confined impinging jet, the details on how the jet-disk separation distance affects the vortex flow structure in the impinging jet flow remains largely unexplored especially when HD_j is above 3.0. In the present study, we continue the work of Hsieh et al. [26] to explore the interactions between the inertia and buoyancy driven vortex rolls for a larger jet-disk separation distance with $HD_j \geq 4.0$. Particular attention will be paid to delineating how the jet-disk separation distance affects the onsets and steady characteristics of the inertia and buoyancy driven vortex rolls. Besides, the influence of HD_j on the onsets of the inertia and buoyancy driven vortex flow instabilities will be explored. Moreover, the characteristics of the time-dependent inertia and buoyancy driven vortex flow affected by HD_j will be unveiled.

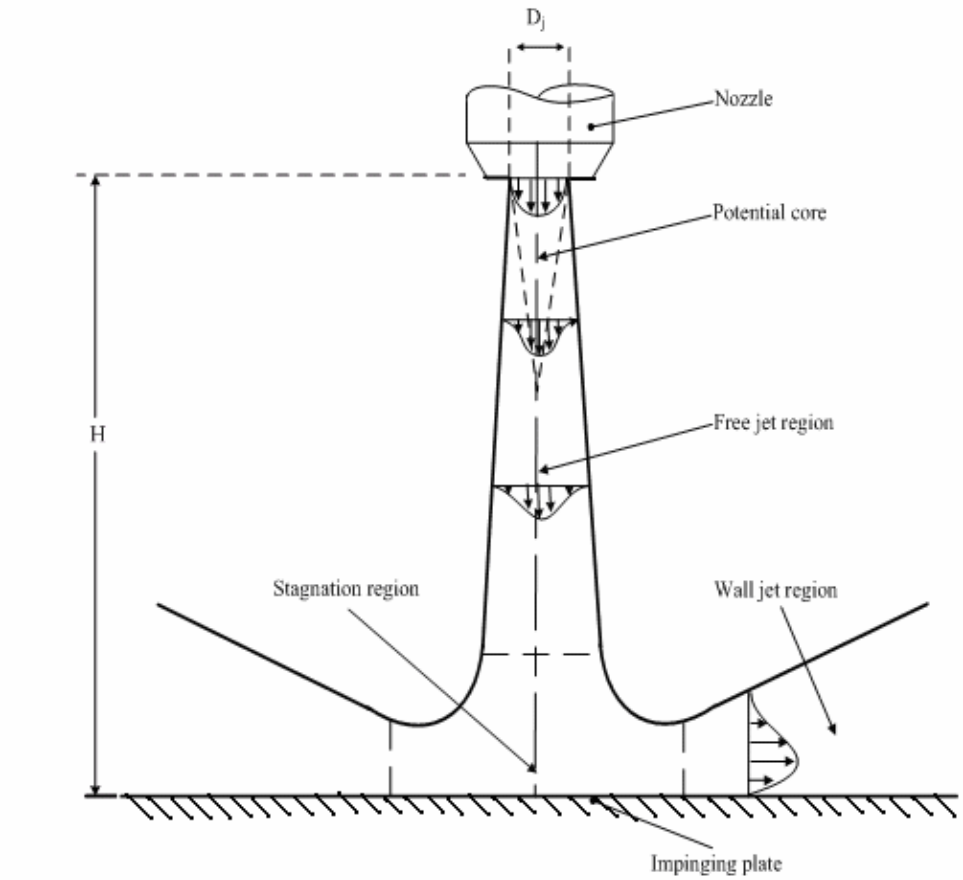

Fig. 1.1 Flow regions associated with a circular jet impinging onto a flat plate.

CHAPTER 2

EXPERIMENTAL APPARATUS AND PROCEDURES

The experimental apparatus and procedures used in the present study to examine how the jet-disk separation distance affects the characteristics of the mixed convective vortex flow resulting from a gas jet impinging onto a horizontal heated disk confined in a vertical cylindrical chamber are modified slightly from those established in our previous study [13]. They are described in the following.

2.1 Experimental Apparatus

A schematic of the experimental system is shown in Fig. 2.1. The test section includes a circular disk held horizontally in a vertical cylindrical chamber with the gas injected vertically downward through a long straight vertical pipe into the chamber. Note that for clear illustration the plots in Fig. 2.1 are not directly proportional to the actual dimensions of the apparatus. In the present experimental study, instead of using inert gases we adopted air as the working fluid intending to save cost of the experiment. The present experimental system consists of four major parts: (1) heating unit, (2) gas injection unit, (3) processing chamber, and (4) flow visualization unit.

(1) Heating unit: The heating unit is designed to maintain the circular disk at the preset uniform temperature during the experiment. It is composed of a 10.0-mm thick copper plate of eight-inch in diameter, acting as the disk, placed above another 20.0-mm thick stationary copper plate of the same diameter, which is heated by D.C. power supplies. The lower copper plate is then placed on a bakelite plate. A gap height of 1 mm is kept between the two copper plates allowing the thermal radiation and convection to transfer heat from the lower to upper plates. The heater attached onto the back side of the lower stationary copper plate is divided into 3 concentric zones

(Fig. 2.2). Each zone is independently heated by a power supply with the D.C. current passing through the nickel coil placed on the stainless steel holder. The entire heating unit is then placed on a Teflon plate. Additionally, to reduce the significant energy loss from the sidewall of the copper plates and Teflon plate, the lateral surface of the entire heating unit is wrapped with a 16.0-mm thick thermal insulation layer of superlon. A proper control of the currents transferred from the power supplies to the heating coils leads to a nearly uniform disk temperature with a maximum deviation of 0.1℃ across the disk. The temperature of the upper copper plate at selected detection points is measured by three T-type thermocouples inserted into the plate by the small holes drilled on the backside of the plate. The locations of the detection points are indicated in Fig. 2.3.

(2) Gas injection unit: The gas injection unit consists of a 2 HP air compressor, a flow meter, a smoke generator, filters, pressure regulator, and connection and injection pipes. In the experiments, the air is drawn from the ambient by the compressor and sent into a 300 liter and 100 psi high-pressure air tank and is filtered to remove moisture and tiny particles. The installation of the high-pressure air tank intends to suppress the fluctuation of the air flow and to extend the life of the compressor. Then, the air is mixed with smoke tracers in the smoke generator and is regulated by the pressure regulator. It is later injected into the processing chamber through the injection pipe which is coaxial with the processing chamber. The downward vertical air jet issuing from the injection pipe exit impinges directly onto the copper disk. In the present study, the injection pipe diameter is fixed at 10.0 mm and the pipe is thermally well insulated by a superlon insulation layer of 16.0-mm thick to prevent heat loss from the compressed air. The straight portion of the pipe is 600.0-mm long. This length of the constant cross-section portion of the injection pipe is selected to ensure that it is long enough to have a fully developed air flow at the

outlet of the injection pipe. The distance between the exit of the injection pipe and the upper surface of the heated disk is varied from 40.0 to 60.0 mm. The air temperature at the cross section 600.0 mm upstream of the injection pipe exit is measured by a T-type thermocouple. The measured value is considered as the temperature of the air injected into the processing chamber in view of the good thermal insulation over the pipe.

(3) Processing chamber: The processing chamber, which is made of 6.0mm-thick quartz glass to allow for the observation of the flow pattern in the chamber, is cylindrical and has a diameter of 291.0 mm. The distance between the chamber top and bottom is 200.0 mm. To facilitate the flow visualization, the chamber top is made of an acrylic plate. Air is injected vertically downward from the injection pipe into the cylindrical chamber and impinges directly onto the heated disk. The air flows fist over the heated disk, then moves through the annular section of the chamber, and finally leaves the chamber via twenty circular outlets of 12.7 mm in diameter opened at the bottom of the chamber. The outside surface of the chamber is thermally well insulated to minimize the heat loss from the processing chamber during the experiment. More specifically, the entire chamber is insulated with a superlon insulator of 10.0-mm thick. The insulator can be opened during the flow visualization experiment.

(4) Visualization unit: A smoke-tracer flow visualization technique is employed to observe the flow patterns induced by the jet impinging onto a heated disk in the cylindrical chamber. The smoke is produced from burning incense prepared from sandalwood. The smoke is mixed uniformly in the smoke generator and is carried out by the inlet air and is sent into the cylindrical chamber. The gas flow pattern in the chamber is illuminated by the vertical and horizontal plane light sheets produced by passing parallel lights from an overhead projector through adjustable knife edges. The experimental system is located in a darkroom to improve the contrast of the flow

visualization. The time variations of the flow pattern from the side views are recorded by the Sony digital video camera DCR-PC330.

(5) Temperature measurement: The air temperature in the processing chamber is measured by inserting a calibrated and corrected thermocouple probe into the chamber through twenty-four holes of 1.0 mm in diameter opened at the selected locations on the top of the chamber. In the experiment, the thermocouple tip is positioned at selected vertical distances from the upper surface of the disk. More specifically, the thermocouple probe is an OMEGA (model HYPO) hypodermic extremely small T-type thermocouple implanted in a 2.0-inch long stainless steel hypodermic needle. The transient air temperature at selected locations in the chamber is recorded by a recorder (YOKOGAWA LR12000E) after the vortex flow reaches a statistical state in which the initial transients in the flow have died out. The sampling rate of the recorder is 9 Hz foe each data channel.

2.2 Experimental Procedures

The experimental parameters included in the present study are the jet-disk separation distance, temperature difference between jet and disk, and jet flow rate. The injection pipe diameter is fixed at 10.0 mm. The temperature difference between jet and disk and jet flow rate are respectively varied from 0 to 25.0℃ and 0 to 12.0 slpm (standard liter per minute) for the jet-disk separation distance varying from 40.0 to 60.0 mm. The experiment starts with the air at the ambient temperature T_a compressed first into a smoke generator through the connection pipes, and then injected into the cylindrical chamber. The air then moves over the heated disk and finally leaves the processing chamber. Meanwhile the temperature of the disk and the air flow rate is controlled at the preset levels. The temporal changes of the flow patterns in the chamber are photographed from the side views successively by the

Sony digital video camera DCR-PC330 for various jet-disk separation distances, gas flow rates, and temperature differences between the disk and inlet air.

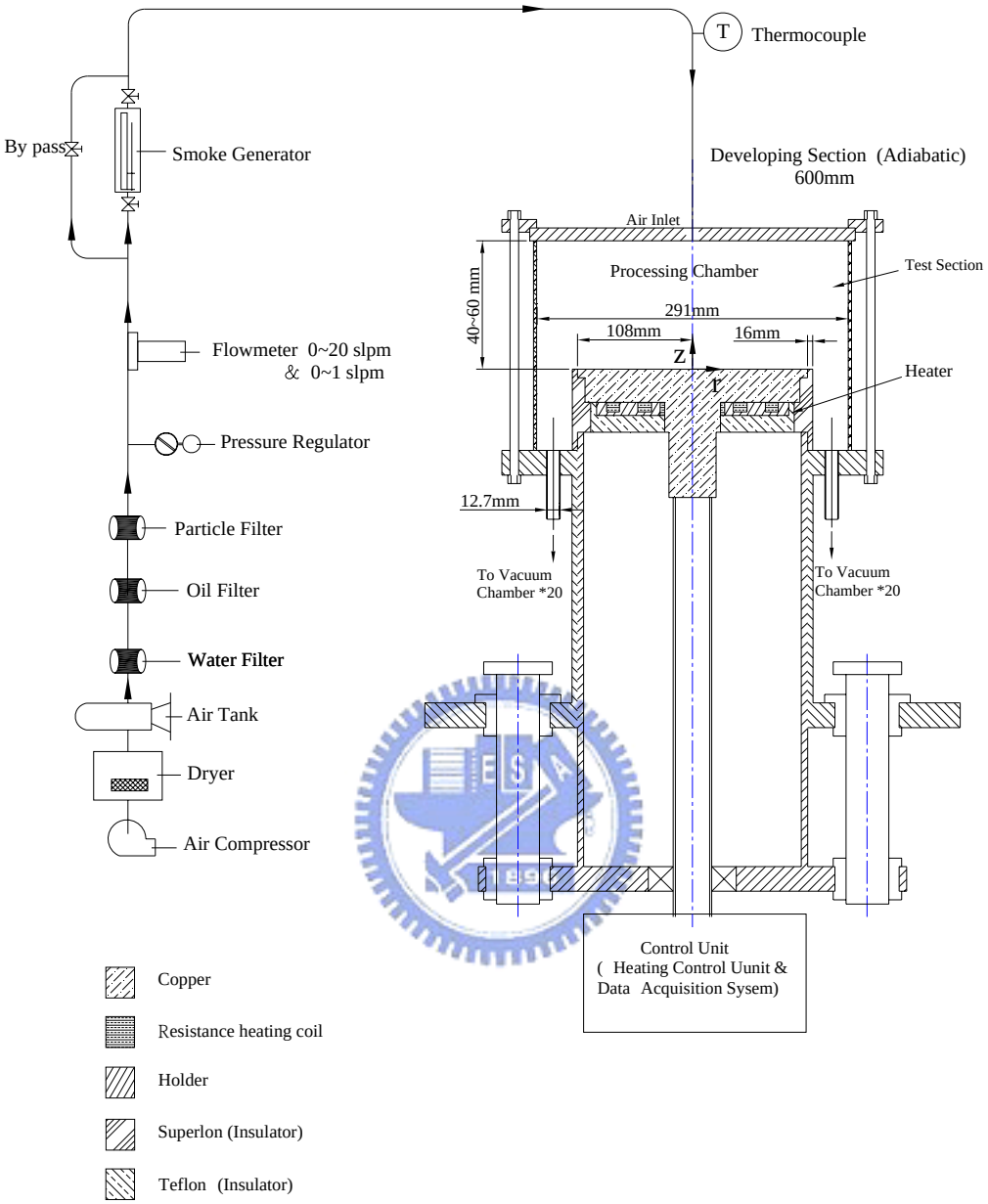

Fig. 2.1 Schematic diagram of the experimental apparatus.

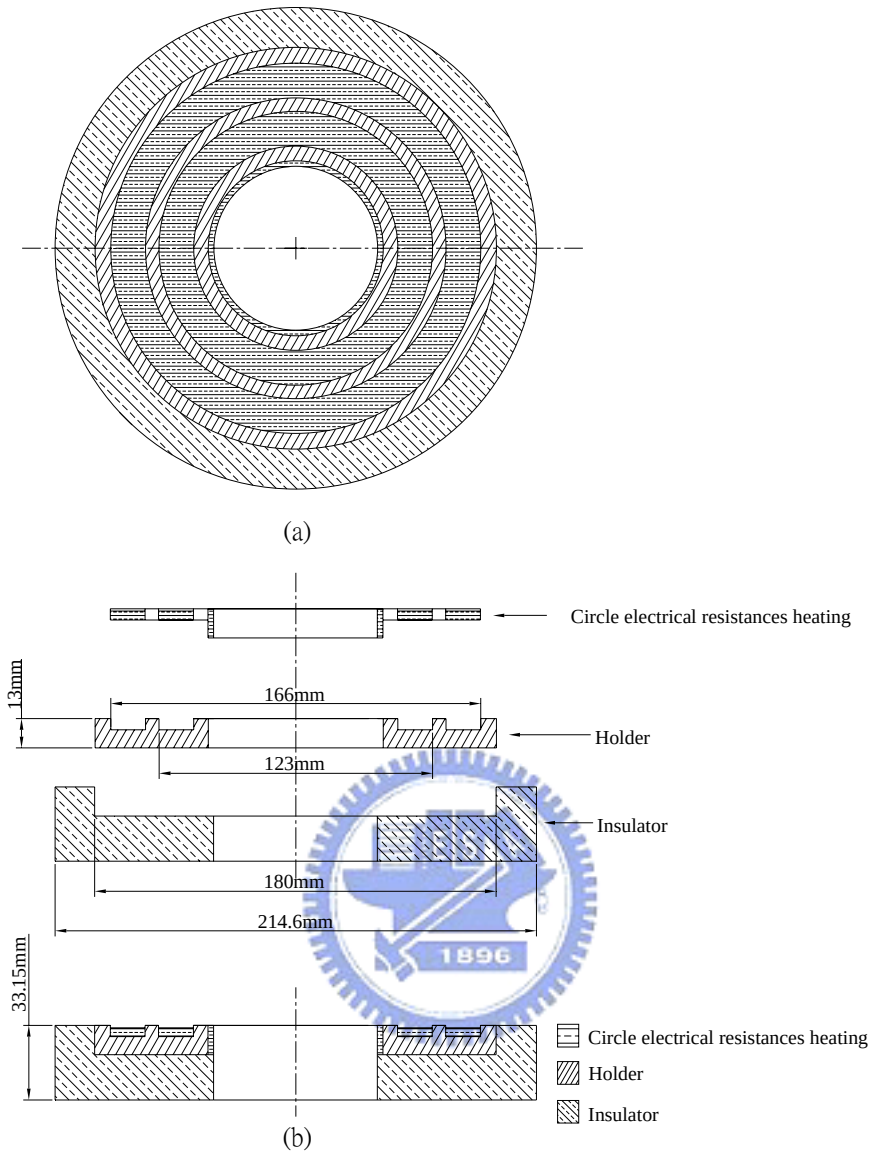

Fig 2.2 The heater consists of three parts: resistance heating element, holder and insulator.

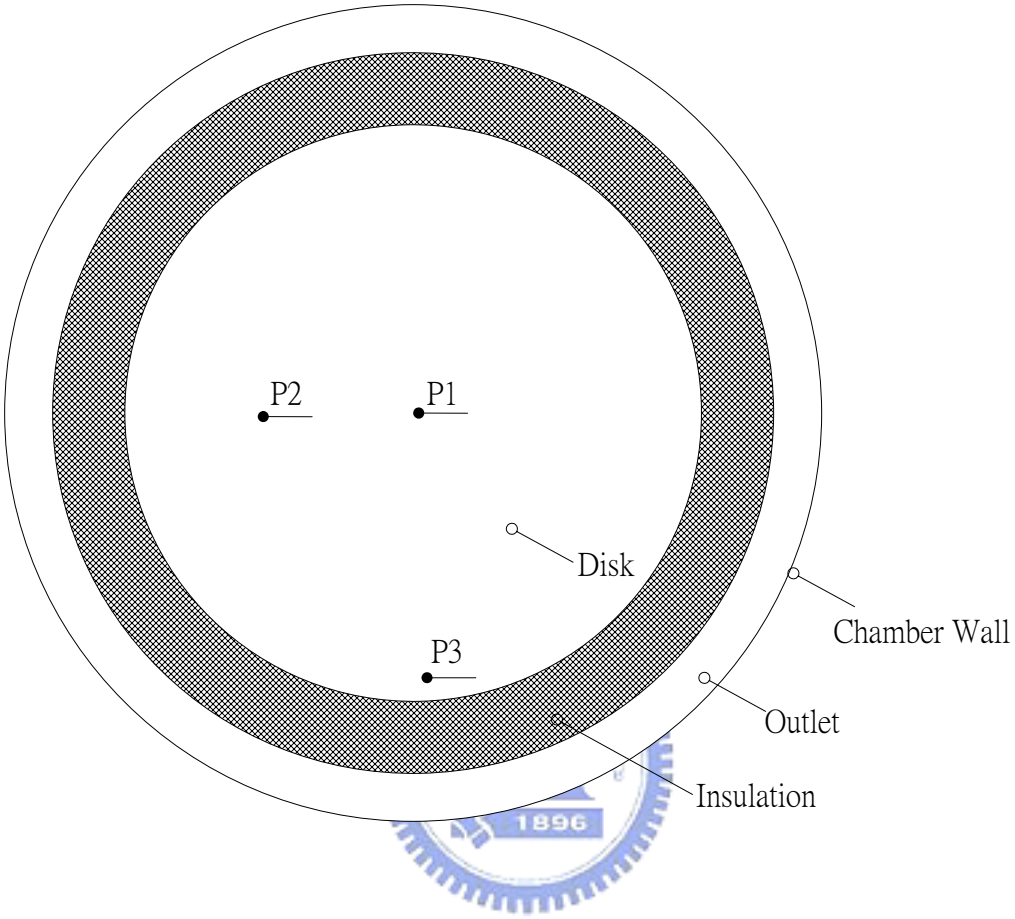

Fig. 2.3 The locations of the detection points on the upper copper plate.

CHAPTER 3

DIMENSIONLESS GROUPS AND UNCERTAINTY ANALYSIS

The dimensionless groups relevant to the present problem and the analysis of the uncertainties of the variables in this experiment are briefly examined in this chapter.

3.1 Dimensionless Groups

The non-dimensional parameters associated with the flow considered here are the ratio HD_j of the jet-disk separation distance H to the diameter of the injection pipe D_j, jet Reynolds number Re_j, based on the average velocity of the air jet $\overline{V}_j$ at the injection pipe exit and the diameter of the injection pipe D_j, and the Rayleigh number Ra, based on the temperature difference between the heated disk and inlet gas ΔT and the jet-disk separation distance H. They are respectively defined as

$$HD_j = \frac{H}{D_j} \tag{3.1}$$

$$Re_j = \frac{V_j D_j}{\nu} = \frac{4}{\pi}\frac{Q_j}{\nu D_j}, \tag{3.2}$$

and

$$Ra = \frac{g\beta(T_f - T_j)H^3}{\alpha\nu} = \frac{g\beta\Delta T H^3}{\alpha\nu} \tag{3.3}$$

where α is the thermal diffusivity, g is the gravitational acceleration, β is the thermal expansion coefficient, and ν is the kinematic viscosity.

3.2 Uncertainty Analysis

An uncertainty analysis is carried out here to estimate the uncertainty levels in the experiment. Kline and McClintock [35] proposed a formula for evaluating the uncertainty in the result F as a function of independent variables, $X_1, X_2, \cdots\cdots\cdots, X_n$,

$$F = F(X_1, X_2, X_3, \cdots\cdots, X_n) \tag{3.4}$$

The absolute uncertainty of F is expressed as

$$\delta F = \left\{ \left[\left(\frac{\partial F}{\partial X_1} \right) \delta X_1 \right]^2 + \left[\left(\frac{\partial F}{\partial X_2} \right) \delta X_2 \right]^2 + \left[\left(\frac{\partial F}{\partial X_3} \right) \delta X_3 \right]^2 + \cdots + \left[\left(\frac{\partial F}{\partial X_n} \right) \delta X_n \right]^2 \right\}^{1/2} \quad (3.5)$$

and the relative uncertainty of F is

$$\frac{\delta F}{F} = \left\{ \left[\left(\frac{\partial \ln F}{\partial \ln X_1} \right) \left(\frac{\delta X_1}{X_1} \right) \right]^2 + \left[\left(\frac{\partial \ln F}{\partial \ln X_2} \right) \left(\frac{\delta X_2}{X_2} \right) \right]^2 + \cdots + \left[\left(\frac{\partial \ln F}{\partial \ln X_n} \right) \left(\frac{\delta X_n}{X_n} \right) \right]^2 \right\}^{1/2} \quad (3.6)$$

If $F = X_1^a X_2^b X_3^c \ldots\ldots$, then the relative uncertainty is

$$\frac{\delta F}{F} = \left[\left(a \frac{\delta X_1}{X_1} \right)^2 + \left(b \frac{\delta X_2}{X_2} \right)^2 + \left(c \frac{\delta X_3}{X_3} \right)^2 + \cdots\cdots \right]^{1/2} \quad (3.7)$$

where $(\partial F / \partial X_i)$ and δX_i are, respectively, the sensitivity coefficient and uncertainty level associated with the variable X_i. The values of the uncertainty intervals δX_i are obtained by a root-mean-square combination of the precision uncertainty of the instruments and the unsteadiness uncertainty, as recommended by Moffat [36]. The choice of the variable X_i to be included in the calculation of the total uncertainty level of the result F depends on the purpose of the analysis. The uncertainties for the chosen parameters are calculated as follows:

(1) Uncertainty of the measured temperature difference, $\Delta T = T_f - T_j$

$$\delta(T_f - T_j) = [(\delta T_f)^2 + (\delta T_j)^2]^{1/2} \quad (3.8)$$

(2) The dependence of the air properties k, μ, and ν on temperature (T in K) [36] is

$$k = 1.195 \times 10^{-6} T^{1.6} / (T + 118)$$

$$\mu = 1.448 \times 10^{-6} T^{1.5} / (T + 118) \quad (3.9)$$

$$\nu = \mu / \rho$$

The uncertainties of the properties are

$$\frac{\delta k}{k}=\frac{T}{k}\frac{\partial k}{\partial T}\frac{\delta T}{T}$$
$$\frac{\delta \rho}{\rho}=\frac{T}{\rho}\frac{\partial \rho}{\partial T}\frac{\delta T}{T} \qquad (3.10)$$
$$\frac{\delta \mu}{\mu}=\frac{T}{\mu}\frac{\partial \mu}{\partial T}\frac{\delta T}{T}$$

(3) Uncertainty of the ratio HD_j,

$$HD_j=\frac{H}{D_j} \qquad (3.11)$$

$$\frac{\delta HD_j}{HD_j}=\left[\left(\frac{\delta H}{H}\right)^2+\left(\frac{\delta D_j}{D_j}\right)^2\right]^{1/2} \qquad (3.12)$$

(4) Uncertainty of the Rayleigh number, Ra,

$$Ra=\frac{g\beta(T_f-T_j)H^3}{\alpha\nu}=\frac{g\beta\Delta TH^3}{\alpha\nu} \qquad (3.13)$$

$$\frac{\delta Ra}{Ra}=\left[\left(\frac{\delta g\beta}{g\beta}\right)^2+\left(3\frac{\delta H}{H}\right)^2+\left(\frac{\delta\Delta T}{\Delta T}\right)^2+\left(\frac{\delta\alpha}{\alpha}\right)^2+\left(\frac{\delta\nu}{\nu}\right)^2\right]^{1/2} \qquad (3.14)$$

(5) Uncertainty of the jet Reynolds number, Re_j,

$$Re_j=\frac{V_jD_j}{\nu}=\frac{4}{\pi}\frac{Q_j}{\nu D_j} \qquad (3.15)$$

$$\frac{\delta Re_j}{Re_j}=\left[\left(\frac{\delta\nu}{\nu}\right)^2+\left(\frac{\delta Q_j}{Q_j}\right)^2+\left(\frac{\delta D_j}{D_j}\right)^2\right]^{1/2} \qquad (3.16)$$

The results from this uncertainty analysis are summarized in Table 3.1.

Table 3.1 Summary of uncertainty analysis

Parameter and Estimate Uncertainty	
Parameters	Uncertainty
D_j, D_w, H (m)	± 0.00005 m
T (℃)	± 0.2℃
ΔT (℃)	±0.3℃
Q_j (slpm)	± 2%
μ (kg/ms) ρ (kg/m^3) υ (m^2/s)	± 0.05% ± 0.05% ± 0.07%
HD_j	± 0.52%
Ra	± 8.6%
Re_j	± 2.3%